Directed Assembly of High Molecular Weight Block Copolymers: Highly Ordered Line Patterns of Perpendicularly Oriented Lamellae with Large Periods

Eunhye Kim,[†] Hyungju Ahn,[†] Sungmin Park,[†] Hoyeon Lee,[†] Moongyu Lee,[‡] Sumi Lee,[‡] Taewoo Kim,[‡] Eun-Ae Kwak,[‡] Jun Han Lee,[‡] Xie Lei,[‡] June Huh,[§] Joona Bang,[⊥] Byeongdu Lee,[‖] and Du Yeol Ryu*,[†]

[†]Department of Chemical and Biomolecular Engineering, Yonsei University, 50 Yonsei-ro, Seodaemun-gu, Seoul 120-749, Korea, [‡]LCD R&D Center, LCD Business, Samsung Display Co., 24 San, Nongseo-dong, Giheung-gu, Yongin 446-711, Korea, [§]Department of Materials Science and Engineering, Yonsei University, 50 Yonsei-ro, Seodaemun-gu, Seoul 120-749, Korea, [⊥]Department of Chemical and Biological Engineering, 5 Anam-dong, Seongbuk-gu, Korea University, Seoul 136-701, Korea., and [‖]X-ray Science Division, Advanced Photon Source, Argonne National Laboratory, 9700 South Cass Avenue, Argonne, Illinois 60439, United States

ABSTRACT The directed assembly of block copolymer nanostructures with large periods exceeding 100 nm remains challenging because the translational ordering of long-chained block copolymer is hindered by its very low chain mobility. Using a solvent-vapor annealing process with a neutral solvent, which was sequentially combined with a thermal annealing process, we demonstrate the rapid evolution of a perpendicularly oriented lamellar morphology in high molecular weight block copolymer films on neutral substrate. The synergy with the topographically patterned substrate facilitated unidirectionally structural development of ultrahigh molecular weight block copolymer thin films—even for the structures with a large period of 200 nm—leading to perfectly guided, parallel, and highly ordered line-arrays of perpendicularly oriented lamellae in the trenched confinement. This breakthrough strategy, which is applicable to nanolithographic pattern transfer to target substrates, can be a simple and efficient route to satisfy the demand for block copolymer assemblies with larger feature sizes on hundreds of nanometers scale.

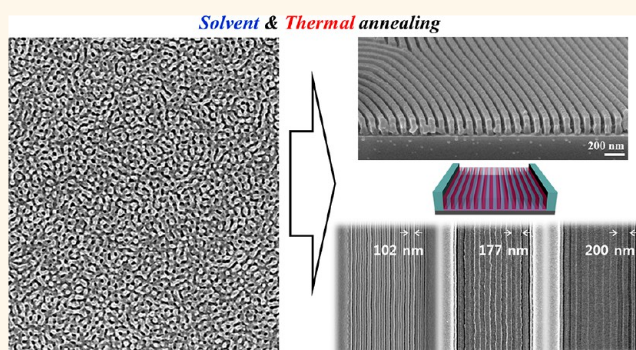

KEYWORDS: high molecular weight · block copolymer · perpendicularly oriented lamellae · exceeding 100 nm · solvent-vapor annealing

The nanoscopic assembly of block copolymer (BCP) thin films is currently of interest as a bottom-up approach for generating templates and scaffolds with well-defined periodic structures of spherical, cylindrical, and lamellar morphologies, typically with a period of 10–50 nm.[1–11] The dimension and morphology of these structures can be dictated by $\chi \cdot N$ as a function of composition, where χ and N are the Flory–Huggins segmental interaction parameter between the two blocks and the total number of segments, respectively.[12,13] Despite a variety of morphologies in BCP nanostructures, spontaneous microphase separation in the thin films leads to the parallel orientation of microdomain arrays or random orientation with defects, which limit the potential applications. These phenomena are attributed to preferential interactions of the substrate with one block and/or the difference in surface energies of the two blocks.[14–16] Much effort has been dedicated to attempts to control the orientation of microdomain arrays in BCP films and to achieve long-range ordered structures using external fields[17–19] or surface modifications.[20–26] For instance, controlling the interfacial and surface interactions afforded a versatile route to direct the perpendicular orientation of cylindrical and lamellar arrays in BCP films, particularly in polystyrene-*b*-poly(methyl methacrylate) (PS-*b*-PMMA) thin films.[14,20–25]

* Address correspondence to dyryu@yonsei.ac.kr.

Received for review July 24, 2012 and accepted February 27, 2013.

Published online February 27, 2013
10.1021/nn3051264

© 2013 American Chemical Society

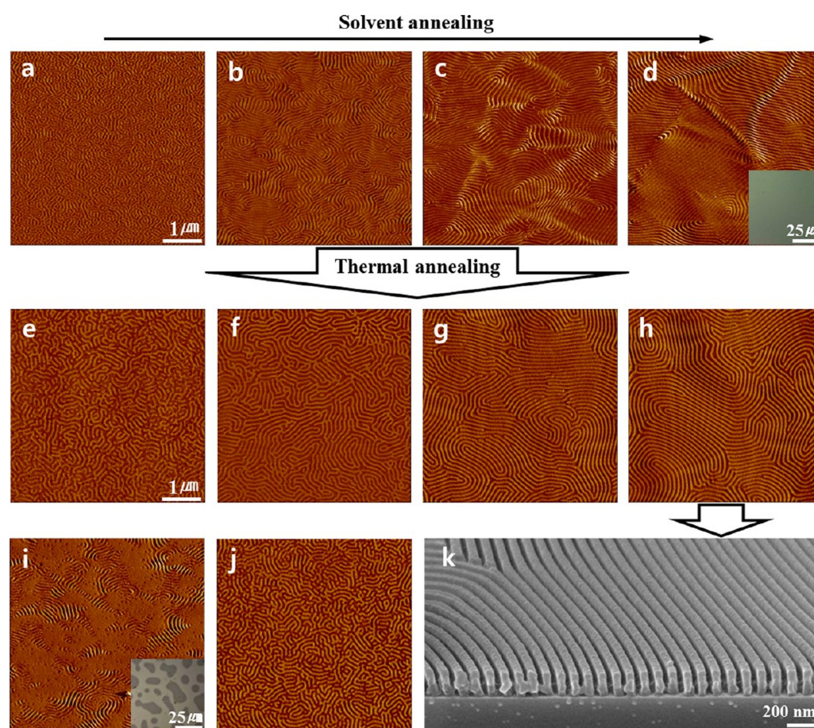

Figure 1. (a–j) AFM phase images of 210-nm-thick PS-*b*-PMMA (M_n = 256 kg/mol) films. The time evolution morphologies on neutral substrate at (a) 10 min, (b) 30 min, (c) 40 min, and (d) 45 min upon solvent-vapor annealing with THF vapor. The insets show the corresponding OM images. Thermally annealed (for 12 h) films at 240 °C after solvent-vapor annealing process for (e) 10 min, (f) 30 min, (g) 40 min, and (h) 45 min. (i) An irregular (or mixed) structure and film dewetting of solvent-annealed (for 30 min) film on the oxide layer of a Si substrate (PMMA-selective substrate). (j) A less-ordered structure in thermally annealed (for 72 h) film at 240 °C under vacuum with no solvent annealing. (k) Tilt-view SEM image of the morphology shown in (h), where the contrast was enhanced by asymmetric dry (or plasma) etching with an O_2/Ar mixture.

In contrast to the successful strategies for sub-10-nm high-density addressable arrays of BCP films,[7,8,27,28] the engineering of BCP films on the intermediate (100–200 nm), hundreds-of-nanometers scale remains challenging both scientifically and technically.[29–31] Developing a method to fabricate such films is crucial, not only to extending feature sizes upward from the nanoscale but also to bridging the unexplored size gap between nano- and microfabrications. The practical demands of photonics and polarizers (in terms of their responses to the visible wavelengths of light) have motivated attempts to generate periodically patterned structures with larger feature sizes (i.e., periods larger than 100 nm).[32,33] The feature size scaling can be directly related to an increase in the molecular weight of the BCP used. However, a notable drawback of this approach is that the translational ordering of high molecular weight BCP is hindered by its very low chain mobility due to highly entangled conformations even at temperatures higher than the glass transition temperature (T_g). To address this issue, an approach using the solvent annealing process[18,27,34–36] can be effective for the development of periodic structures in high molecular weight BCP films.

In this work, our approach exploited a solvent-vapor annealing process using tetrahydrofuran (THF) that is a nonselective good solvent for the two blocks of PS-*b*-PMMA. The structural development of lamellar morphology was studied in high molecular weight PS-*b*-PMMA films. Herein, we present a simple, versatile, and accelerated route to fabricate extremely ordered line patterns of a perpendicularly oriented lamellar morphology with large periods exceeding 100 nm, which were aligned in parallel with the topographic line patterns. This feasible approach differs from previous studies (the solvent selectivity to the blocks was controlled for various morphologies),[16,19,37,38] in that a solvent-vapor annealing process with neutral solvent was applied to BCP films to direct the orientation of larger microdomain arrays, and it was sequentially combined with thermal annealing process to provide a desired morphology.

RESULTS AND DISCUSSION

Parts a–j of Figure 1 show atomic force microscopy (AFM) phase images of solvent-annealed, 210-nm-thick PS-*b*-PMMA (M_n = 256 kg/mol) films on neutral substrate at constant 10 °C. In the AFM images, the darker and brighter phases correspond to the PS and PMMA blocks, respectively; this difference in brightness is due to the viscoelastic contrast between the two blocks.[14] Upon solvent-vapor annealing, THF vapor was readily absorbed into the film, and the ordering of the microphase in swollen BCP films was

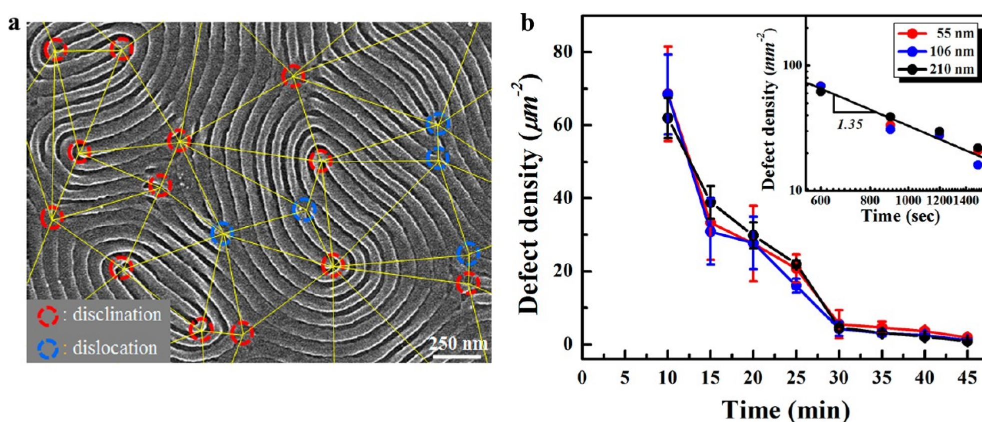

Figure 2. (a) In-plane SEM image of solvent-annealed (for 35 min), 55-nm-thick PS-*b*-PMMA (M_n = 256 kg/mol) film. Defects in the striped patterns were analyzed in an area of 5 × 5 μm^2 *via* the automatic triangulation program of the distances between neighboring defects. Spontaneous dislocations and disclinations (terminal points, junctions, and dots) in the perpendicular geometry of the lamellar planes are indicated with the blue and red colors in the image, respectively. (b) The averaged defect density (ρ) as a function of solvent-vapor annealing time at constant 10 °C for the films with thickness of 55, 106, and 210 nm. The inset shows a log−log plot up to 25 min, indicating that a solvent-vapor annealing process with a neutral solvent exhibited a very fast value (ν = 1.35) for the kinetic exponent, by the power law of $\rho \sim t^{-\nu}$.

significantly enhanced by an increase in the chain mobility. The selectivity ratio of THF to the PS and PMMA was evaluated to be 1.125 from the saturated thickness of each homopolymer film, as determined by a solvent absorption experiment (see Figure S1, Supporting Information). This result indicates that THF is a nonselective (or neutral) good solvent for the two blocks of PS-*b*-PMMA and has little influence on the volume fraction of BCP. With increasing annealing time, the early stage surface morphology (Figure 1a) evolved into long and striped patterns in a lamellar morphology (Figure 1d), with no film dewetting (the inset OM image of Figure 1d) at 45 min exposure. The solvent-vapor annealing process enabled the translational ordering of long-chained (or high molecular weight) BCP, resulting in the perpendicular orientation of lamellar morphology. An optimum annealing time with solvent vapor was dependent on temperature in the closed chamber; this optimum time shortened from 45 min at 10 °C to 25 min at 30 °C. As shown in parts a−d of Figure 1, this process tends to annihilate the defects in the striped patterns, but it leaves ridges on the film surface. However, when the solvent-annealed PS-*b*-PMMA films were thermally annealed at 240 °C for 12 h under vacuum, the AFM images show the ridgeless and highly contrasting morphology in which the film topology is broadly stabilized (parts e−h of Figure 1). Most defects were effectively annihilated during solvent-vapor annealing, rather than thermal annealing process.

The films on the oxide layer of a Si substrate (Figure 1i, and the inset OM image for comparison) exhibited an irregular or mixed structure as well as film dewetting at an earlier time (30 min), despite the fact that the layer was PMMA-selective. Considering that all BCP films upon solvent-vapor annealing may dewet eventually with long time exposure to THF, it can be concluded that the polymeric brushes on neutral substrate significantly delayed film dewetting. Consequently, the use of neutral substrate with poly(styrene-*r*-methyl methacrylate) (P(S-*r*-MMA)) copolymer brushes is a key step to balance the interfacial interactions of the substrate toward the PS and PMMA blocks and suppresses film dewetting. In contrast, when the same PS-*b*-PMMA film was thermally annealed at 240 °C for 72 h (or 12 h) under vacuum with no solvent-vapor annealing, a less ordered structure (Figure 1j) was produced, indicating that the molecular weight was too high to overcome the local free energy barriers associated with the defect annihilation. Figure 1k also displays a tilt-view scanning electron microscopy (SEM) image of the morphology shown in Figure 1h, where the contrast was enhanced by asymmetric dry (or plasma) etching with an O_2/Ar (5/1 in volume ratio) mixture. The internal structure in the SEM image confirms that the thermally annealed PS-*b*-PMMA films with an optimum solvent-vapor annealing (45 min) exhibited a perpendicularly orientated lamellar morphology with long-range lateral order.

To assess the in-plane morphology of solvent-annealed PS-*b*-PMMA (M_n = 256 kg/mol) films, defects including dislocations and disclinations were statistically analyzed in a large area of 5 × 5 μm^2, *via* the automatic triangulation program of the distances between neighboring defects. The 10 areas in each film were randomly selected for the defect analysis. Figure 2a illustrates the SEM image analysis of the striped patterns for solvent-annealed (for 35 min), 55-nm-thick PS-*b*-PMMA film. Spontaneous dislocations and disclinations (terminal points, junctions, and dots) are shown in the perpendicular geometry of the lamellar planes, as indicated with the blue and red colors in the image, respectively.[39−41] Figure 2b shows the averaged defect density (ρ) as a function of

annealing time. During solvent-vapor annealing of the films with thicknesses of 55, 106, and 210 nm, the defect density in PS-*b*-PMMA films decreased rapidly to ~5 μm^{-2} at the first 30 min, which arose from the coarsening of the short line patterns of perpendicularly oriented lamellae. With further annealing to 45 min, the defect density remarkably reduced to ~1 μm^{-2}, as the few defects were annihilated in a pairwise fashion.

According to coarsening dynamics, the process generally follows the power law

$$\rho \approx t^{-\nu} \quad (1)$$

where ν is the kinetic exponent.[42] In the striped patterns consisting of single-layered cylinders, the thermal annealing of BCP films led to a value of $\nu = 0.5$.[39] However, the (neutral) solvent-vapor annealing process at constant 10 °C exhibited a very fast value of $\nu = 1.35$, as shown by the inset in Figure 2b, although it was readily tunable by controlling temperature in the closed chamber. The rapid defect annihilation in the early stages can be explained by two main effects: first, the slow (reptation) dynamics of highly entangled polymer chains was accelerated by the absorption of solvent vapor into BCP films; second, the free energy barriers (Δf^*) in the local energy landscape (the pathway barriers to the formation of well-ordered structures) became shallower to overcome by $\Delta f^* \sim (\phi\chi)N$ due to the dilution approximation, where ϕ is the volume fraction of polymer.[43] Particularly in high molecular weight (high-*N*) BCP films, these effective driving forces for ordering dominate compared to the loss of driving force from dilution by the neutral solvent.

Grazing-incidence small-angle X-ray scattering (GISAXS) was also used to characterize the structures of BCP films, providing macroscopic information over a large area of 2 × 2 cm^2. In the grazing incidence scattering geometry, α_f and $2\theta_f$ are the exit angles of the X-ray beam along the out-of-plane scattering normal to the sample surface and along the in-plane scattering normal to the incidence plane (or parallel to the sample surface), respectively, where $q = (4\pi/\lambda)\sin\theta_f$ is the scattering vector. The incident angle (α_i) was set at 0.180°, which is above the critical angle (0.156°) for PS-*b*-PMMA films, to probe the film morphology across the entire thickness. Figure 3a shows the GISAXS pattern for solvent-annealed (for 45 min), 210-nm-thick PS-*b*-PMMA film on the substrate. A perpendicular geometry produced the Bragg rods at $2\theta_f = 0.122°$ ($q = 0.079$ nm^{-1}) along the out-of-plane scattering and the weak higher order peaks along the horizon of $\alpha_f = 0.200°$, whereas for 55-nm-thick PS-*b*-PMMA film they were markedly shown due to the thickness effect (see Figure S2, Supporting Information). A plot of the line scans along the horizon of $\alpha_f = 0.200°$ (taken from the GISAXS patterns) is shown in Figure 3c for various annealing times. The time evolution of PS-*b*-PMMA films with solvent vapor indicates the structural development of BCP films by an increase in the intensities of the primary peaks (at q^*) and the higher order peaks at $q/q^* = 1:2:3$.

However, when the solvent-annealed (for 45 min) PS-*b*-PMMA film was thermally annealed, as shown in Figure 3b, the Bragg rods at $2\theta_f = 0.096°$ ($q = 0.062$ nm^{-1}) intensified and noticeably elongated along the out-of-plane scattering with the narrow width at half-maximum of the primary peak, indicating a significant improvement in the perpendicular orientation of lamellar morphology with long-range lateral order. It was also confirmed by the line scan shown in Figure 3c, in which many higher order peaks at $q/q^* = 1:2:3:4:5:6:7:8:9$ were identified. The higher intensities of the odd-integer-numbered peaks are attributed to the volumetric symmetry between the two blocks in the thermally equilibrated state.

The inset in Figure 3c shows the *d*-spacing ($d = 2\pi/q^*$) and *in situ* swelling of PS-*b*-PMMA films as a function of annealing time during solvent-vapor annealing process. The *d*-spacing increased from 73.6 to 78.8 nm on annealing for 25 min, but with further annealing time it approached to a plateau value of 78.8 nm, which was assumed to be the quasi-equilibrium *d*-spacing of solvent-annealed BCP films due to the dilution approximation. When all of these solvent-annealed PS-*b*-PMMA films were thermally annealed at 240 °C for 12 h under vacuum, the *d*-spacings recovered into a value of 102 nm, as indicated in the inset. The *d*-spacing of the semidiluted BCP processed with a neutral solvent can be theoretically interpreted by the power law

$$d \approx \phi^{\beta} \quad (2)$$

where $\beta \approx 0.22$ in the strong segregation regime.[44] The swelling behavior of BCP film (as shown by the light *x*-axis of the inset in Figure 3c) enabled us to calculate a value of $\phi = 0.33$ (67% solvent) at equilibrium, using $\phi = 1/\alpha_N = 1/(t/t_0)$ at a plateau normalized thickness ($t/t_0 = 3.0$), where α_N is the swelling ratio in the film geometry. The predicted *d*-spacing (78%) at $\phi = 0.33$ was in good agreement with the observed reduction (77%) in *d*-spacing. This complete recovery into a thermal equilibrium *d*-spacing indicates that the solvent-annealed BCP films were thermally re-equilibrated by increasing short-range segregation between the two blocks (irrespective of annealing time with solvent vapor), while most defects were effectively annihilated during solvent-vapor annealing process as shown in Figure 1. This combinational process is therefore worthy of note, in the sense that the thermal annealing of optimally solvent-annealed BCP films resulted in a uniform structure of a perpendicularly oriented lamellar morphology over the entire films; in addition, this coprocess was highly reproducible as a generalized approach for high molecular weight BCP films.

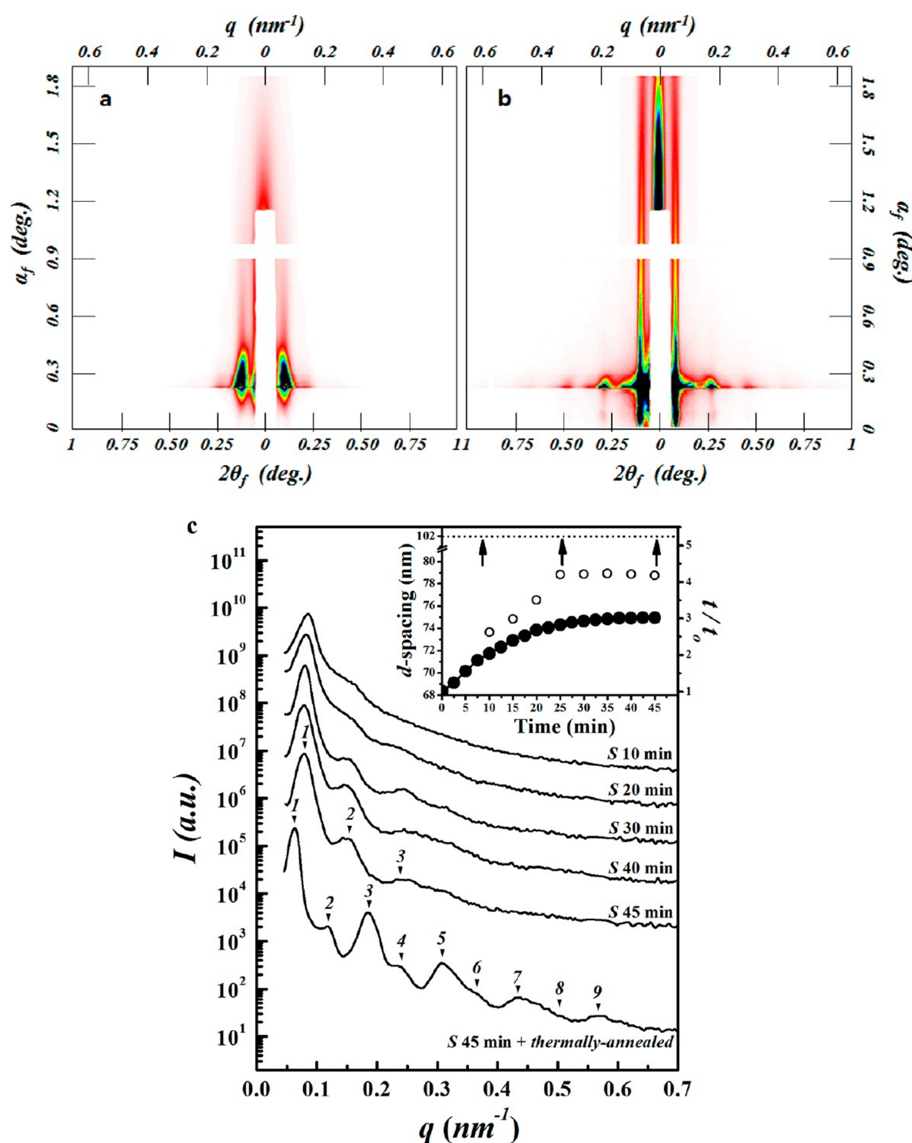

Figure 3. GISAXS patterns for (a) solvent-annealed (for 45 min), 210-nm-thick PS-*b*-PMMA film on the substrate, which is the same film shown in Figure 1d, and (b) thermally annealed (for 12 h) films at 240 °C after solvent annealing process for 45 min, which is the same film shown in Figure 1g. (c) The line scans along the horizon of α_f = 0.200°, taken from the GISAXS patterns, where the *S* denotes to solvent-annealed films. The inset shows the *d*-spacing ($d = 2\pi/q^*$; ○) and *in situ* swelling (t/t_0; ●) of PS-*b*-PMMA films as a function of solvent-vapor annealing time. The arrows represent the complete recovery into a thermal equilibrium *d*-spacing of 102 nm, irrespective of annealing time with solvent vapor.

We further examined the lateral alignment of lamellar morphology in the topographic (or graphoepitaxial) confinement, which was prepared on an underlying layer of neutral substrate using an I-line photolithography process with a negative photoresist (SU-8). The solvent-annealed PS-*b*-PMMA (M_n = 256 kg/mol) film in 1.5 μm wide topographic line patterns was then thermally annealed at 240 °C for 3 h under vacuum in combination using the similar route as described above. As shown in Figure 4a, an in-plane SEM image of 120-nm-thick PS-*b*-PMMA film displays the highly ordered line-arrays of perpendicularly oriented lamellae, which were laterally aligned parallel to the trench walls with fidelity (the inset tilt-view SEM image). This behavior is attributed to the PS-selective, cross-linked polymer trench walls and the neutral bottom toward the two blocks of PS-*b*-PMMA because the PS block wets both trench walls and the parallel alignment propagates into the centers of the line patterns. The lengths in the inset indicate the film thicknesses before (120 nm) and after (70.9 nm) asymmetric dry etching in a trench depth (258 nm). When the contrast was enhanced by asymmetric dry etching that predominantly eliminated the PMMA block, the two end-walls and 13/14 lines of the PS block (with 48/52 ratio) were seen in every trench, indicating that the lamellar period (L_0 = 102 nm) was commensurate with a trench width of 1.5 μm, as the fit within the trenches was achieved by either stretching or compression of the block chains in BCP films.

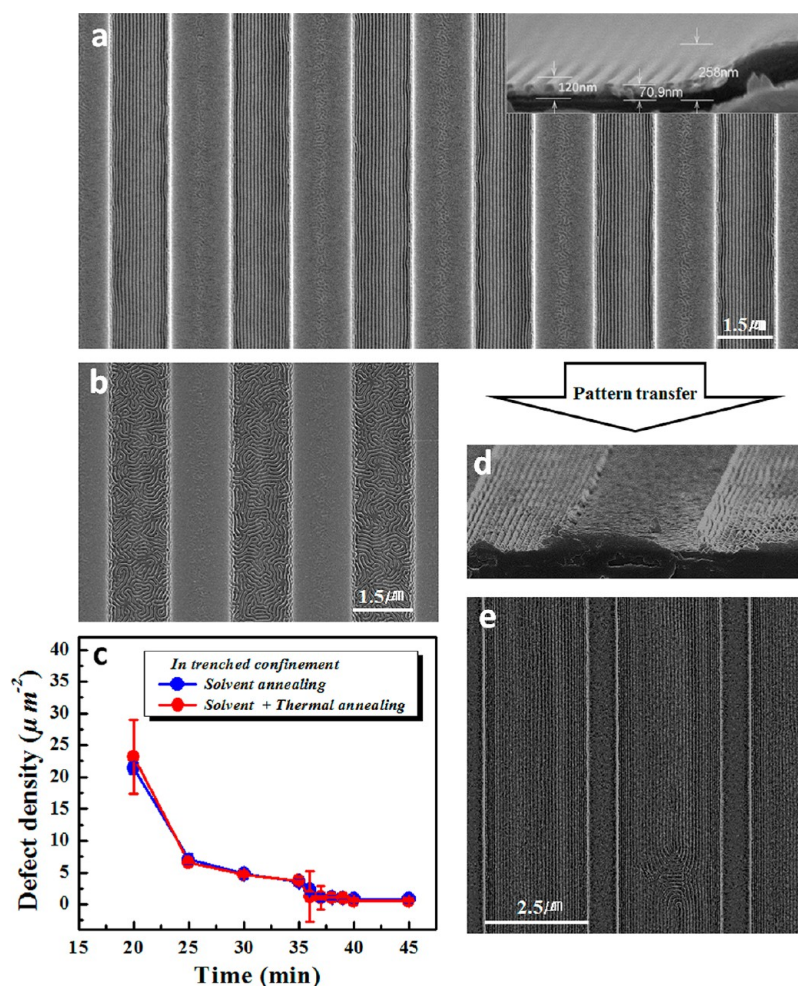

Figure 4. In-plane SEM images of templated, 120-nm-thick PS-*b*-PMMA (M_n = 256 kg/mol) films in the topographic confinement with (a) 1.5 μm width and (e) 2.5 μm width, which were prepared by the combinational process (the thermal annealing of optimally solvent-annealed BCP films). The contrast was enhanced by asymmetric dry etching that predominantly eliminated the PMMA block. The inset shows tilt-view SEM image of (a). (b) Thermally annealed BCP film (with no solvent-vapor annealing) at 240 °C for 12 h under vacuum. (c) The averaged defect density (ρ) for PS-*b*-PMMA films in a 1.5-μm-wide trenched confinement as a function of annealing time with solvent vapor, where the solvent-annealed BCP films were then thermally annealed at 240 °C for 3 h under vacuum for comparison. (d) Silicone oxide pattern substrate manipulated by nanolithographic pattern transfer using templated PS-*b*-PMMA (M_n = 256 kg/mol) film in a 1.5 μm wide topographic line pattern (a).

When the same PS-*b*-PMMA film was thermally annealed at 240 °C for 12 h under vacuum with no solvent-vapor annealing, as shown in Figure 4b, a less ordered structure in every trench confirms its very low chain mobility in high molecular weight BCP film. Figure 4c shows the averaged defect density (ρ) for PS-*b*-PMMA films in a 1.5-μm-wide trenched confinement as a function of annealing time with solvent vapor, where the solvent-annealed BCP films were then thermally annealed at 240 °C for 3 h under vacuum for comparison. The AFM images were analyzed as shown in Figure 2. During solvent-vapor annealing of BCP films in the trenches, the defect density decreased rapidly to $\sim$7 μm^{-2} at 25 min and then approached to $\sim$1 μm^{-2} for 37 min, which were earlier than those in solvent-annealed planar films due to accelerated defect annihilation by the trench walls. When the solvent-annealed PS-*b*-PMMA films in the trenches were thermally annealed, however, there was little improvement in defect density, confirming that most defects were effectively annihilated during solvent-vapor annealing process. The same combinational process of BCP film was applied to a large 2.5-μm-wide topographic line patterns, as shown in Figure 4e by an in-plane SEM image of templated PS-*b*-PMMA (M_n = 256 kg/mol) film. Most line-arrays of perpendicularly oriented lamellae were laterally aligned parallel to the trench walls, though minor in the defects, presumably indicating the limitation of trench width for the propagating lamellar alignment.

The minimum thermal annealing time at 240 °C was measured to be only 2 h due to the effective ordering of the microphase in BCP films during solvent-vapor annealing process. Moreover, the process in a large

area of 3 × 3 cm^2 for laboratory purpose was successful (Figure S3, Supporting Information), indicating a promising scalability for practical purpose. Consequently, the synergistic combinational process that exploits the topography facilitated unidirectionally structural development of high molecular weight BCP films in a bottom-up approach, leading to perfectly guided perpendicular orientation of lamellae in the line confinement. Note that this fabrication method is amenable to the demands for bent or complex line patterns, and it is not limited to straight-line patterns.[45−52] For application purposes, the templated line patterns of perpendicularly oriented lamellae can be used as a well-defined mask in a reactive ion etching (RIE) process. More specifically, a silicone oxide pattern substrate was manipulated by nanolithographic pattern transfer using templated PS-*b*-PMMA (M_n = 256 kg/mol) film in a 1.5-μm-wide topographic line pattern (Figure 4a), as demonstrated in Figure 4d. It can be also applied as a top-down approach to manufacture in-cell polarizers for liquid crystal displays (LCD) that require hundreds-of-nanometers scale in pitch.[53,54]

To ascertain the versatility and general applicability for this strategy, two symmetric ultrahigh molecular-weight PS-*b*-PMMAs (M_n = 733 and 1000 kg/mol) were used in a similar process. For thermally annealed BCP films at 240 °C for 12 h with no solvent-vapor annealing, the SEM images exhibited a less developed structure in every trench, as shown in parts a and b of Figure 5. The solvent-vapor annealing time was increasingly applied to higher molecular weight BCP films: 90 min and 10 h for the PS-*b*-PMMAs having M_n = 733 and 1000 kg/mol, respectively, because the ordering of ultrahigh molecular weight BCPs was more seriously hindered by the limited chain mobility. Nevertheless, when the solvent-annealed PS-*b*-PMMAs films were thermally annealed, long-range ordered lamellar structures were achieved, as shown in Figure S4 (Supporting Information) by the SEM images of 360-nm-thick PS-*b*-PMMA (M_n = 1000 kg/mol) film. Parts c and d of Figure 5 show in-plane SEM images of templated PS-*b*-PMMAs (M_n = 733 and 1000 kg/mol, respectively) films in a 1.5-μm-wide topographic line pattern by the combinational process (the thermal annealing of optimally solvent-annealed BCP films). In these cases, the giant lamellae correspond to L_0 = 177 and 200 nm, respectively, in the superstrong segregation regime. A visible variation in line width of the PS-*b*-PMMAs (M_n = 1000 kg/mol) films is attributed to asymmetric dry (or plasma) etching of slightly concaved film in thickness, because a consistent line width of the same film without etching was observed by the AFM image. Thus, the similar results with the PS-*b*-PMMA (M_n = 256 kg/mol) films were seen in the trenched confinement, consisting of perpendicularly oriented giant lamellae. This simple and feasible strategy facilitated the directed assembly of periodically

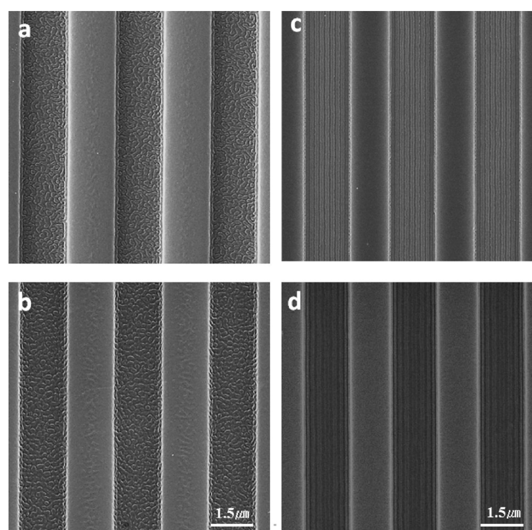

Figure 5. In-plane SEM images of templated, 100-nm-thick PS-*b*-PMMA films in the topographic confinement with 1.5 μm width. Thermally annealed PS-*b*-PMMA films (with no solvent-vapor annealing) at 240 °C for 12 h under vacuum for (a) M_n = 733 kg/mol and (b) M_n = 1000 kg/mol. BCP films prepared by the combinational process for (c) M_n = 733 kg/mol and (d) M_n = 1000 kg/mol, where the solvent-annealed BCP films were thermally annealed at 240 °C for 3 h under vacuum. Contrast was enhanced by asymmetric dry etching that predominantly eliminated the PMMA block.

patterned structures even in ultrahigh molecular weight BCP films with feature sizes on a hundreds-of-nanometers scale.

CONCLUSIONS

In summary, we demonstrated the rapid evolution of a perpendicularly oriented lamellar morphology in high molecular weight PS-*b*-PMMA ($M_n \geq$ 256 kg/mol) films using a solvent-vapor annealing process with neutral solvent, where the interfacial interactions of the substrate were balanced by grafting P(S-*r*-MMA) copolymer brushes. When the solvent-vapor annealing process for BCP films was sequentially combined with thermal annealing process, this combinational approach resulted in a uniform and perpendicularly oriented lamellar morphology with long-range order over the films.

The synergy with the topographically patterned substrate facilitated unidirectionally structural development of high molecular weight BCP films in a bottom-up approach; this led to perfectly guided, parallel, and extremely ordered line-arrays of perpendicularly oriented lamellae in the trenched confinement. For further applications in ultrahigh molecular weight PS-*b*-PMMA films, our strategy may have significant implications for scaling to dimensions with large periods exceeding 200 nm.[32,33] The extension of BCP lithography to larger feature sizes on hundreds-of-nanometers scale creates opportunities for the widespread use of the unexplored size scales between nano- and microfabrications as well as many different

types of practical demands. This strategy, which is highly reproducible and compatible with nanolithographic pattern transfer for photonics and polarizers, can be a simple and feasible route to fabricate the directed assembly of the periodically patterned, large-featured structures in high molecular weight BCP films.

METHODS

Synthesis and Sample Preparation. Three symmetric PS-*b*-PMMA copolymers with a PS volume fraction (ϕ_{PS}) of 0.500 were synthesized *via* sequential anionic polymerization of styrene and methyl methacrylate in tetrahydrofuran (THF); this was performed at −78 °C in the presence of LiCl (high purity, Aldrich), under purified argon, and using *sec*-butyllithium as an initiator. The number-averaged molecular-weights (M_n), as characterized by size-exclusion chromatography (SEC), were 256, 733, and 1000 kg/mol, with a narrow molecular weight distribution (less than 1.07). Their equilibrium periods (or interlamellar spacings, L_0) of BCPs were measured to be 102, 177, and 200 nm, respectively. The PS-*b*-PMMA films were prepared by spin-coating typically at 3000−5500 rpm for 60 s; 1−4 wt % BCP solutions in toluene were applied to the substrates to control the film thickness.

A neutral substrate was prepared using a hydroxyl end-functionalized poly(styrene-*r*-methyl methacrylate) (P(S-*r*-MMA)) with a styrene mole fraction (X_S) ~ 0.56 and M_n = 15000 g/mol (Polymer Source, Inc.).[20] The surface modification by grafting reaction to the substrate was accomplished by thermally annealing P(S-*r*-MMA) films on Si wafers at 170 °C for 3 days under vacuum; this temperature is well above the glass transition temperatures (T_g's) of PS and PMMA (100 and 115 °C, respectively). The grafting thickness of random copolymer was measured to be ~5.5 nm by ellipsometry (SE MG-1000, Nanoview Co.) at an incidence angle of 70° after rinsing with toluene to remove the unanchored polymer chains from the substrate. The topographic line patterns were prepared on an underlying layer of neutral substrate using an I-line photolithography process with a negative photoresist (SU-8; Microchem).

A neutral solvent of tetrahydrofuran (THF; high purity, Aldrich) was used for solvent-vapor annealing of PS-*b*-PMMA films. A cylindrical bronze chamber was devised to set the volume (V = 706.5 cm^3) and surface area (S = 78.5 cm^2) of the solvent, where the solvent uptake in the films was precisely controlled by the annealing time, under the condition of S/V = 0.111 cm^{-1}. The chamber was completely sealed by Teflon cap with Chemraz (Greene Tweed Co.) O-ring. The temperature in the closed chamber was set at constant 10 °C for long enough time. It is important for reproducibility to maintain a constant temperature inside and outside chamber. For nanolithographic pattern transfer, the reactive ion etching (RIE; Oxford) mode was operated with SF_6 by a RF power of 200 W at 30 mtorr and 30 sccm. To enhance the phase contrast between the two blocks in PS-*b*-PMMA films, asymmetric dry (or plasma) etching (VITA, Femto Sci.) mode was operated with an O_2/Ar (5/1 in volume ratio) mixture by a RF power of 100 W at 150 mtorr and 18 sccm.

Characterization of BCP Films. Grazing-incidence small-angle X-ray scattering (GISAXS) experiments were performed at the 8-ID-E beamline of the Advanced Photon Source (APS) at Argonne National Laboratory and the 3C beamline at Pohang Accelerator Laboratory (PAL), Korea. The operating conditions were chosen as a wavelength of 1.69 Å and a sample-to-detector distance of 2.2 m. The incident angle (α_i) was set at 0.180°, which is above the critical angle (0.156 °) for PS-*b*-PMMA films. To examine the surface morphology of PS-*b*-PMMA films, atomic force microscopy (AFM; Dimension 3100, Digital Instrument Co.) was operated in the tapping mode, and field emission scanning electron microscopy (FESEM; S-4800, Hitachi) was used with an accelerating voltage of 5.0 kV.

Conflict of Interest: The authors declare no competing financial interest.

Acknowledgment. This work was supported by Samsung Electronics with a partial aid of National Nanofab Center (NNFC), Korea. We also acknowledge support from the Nuclear R&D Programs, APCPI ERC (R11-2007-050-00000), and Converging Research Center (2010K001430) funded by the Ministry of Education, Science & Technology (MEST), Korea.

Supporting Information Available: Solvent absorption of homopolymers, supplementary AFM phase images, GISAXS patterns, and SEM images. This material is available free of charge *via* the Internet at http://pubs.acs.org.

REFERENCES AND NOTES

1. Park, M.; Harrison, C.; Chaikin, P. M.; Register, R. A.; Adamson, D. H. Block Copolymer Lithography: Periodic Arrays of ~10^{11} Holes in 1 Square Centimeter. *Science* **1997**, *276*, 1401–1404.
2. Thurn-Albrecht, T.; Schotter, J.; Kastle, G. A.; Emley, N.; Shibauchi, T.; Krusin-Elbaum, L.; Guarini, K.; Black, C. T.; Tuominen, M. T.; Russell, T. P. Ultrahigh-Density Nanowire Arrays Grown in Self-Assembled Diblock Copolymer Templates. *Science* **2000**, *290*, 2126–2129.
3. Cheng, J. Y.; Ross, C. A.; Chan, V. Z. H.; Thomas, E. L.; Lammertink, R. G. H.; Vancso, G. J. Formation of a Cobalt Magnetic Dot Array *via* Block Copolymer Lithography. *Adv. Mater.* **2001**, *13*, 1174–1178.
4. Lazzari, M.; López-Quintela, M. A. Block Copolymers as a Tool for Nanomaterial Fabrication. *Adv. Mater.* **2003**, *15*, 1583–1594.
5. Tang, C.; Lennon, E. M.; Fredrickson, G. H.; Kramer, E. J.; Hawker, C. J. Evolution of Block Copolymer Lithography to Highly Ordered Square Arrays. *Science* **2008**, *322*, 429–432.
6. Jeong, S.; Xia, G.; Kim, B. H.; Shin, D. O.; Kwon, S.-H.; Kang, S.-W.; Kim, S. O. Universal Block Copolymer Lithography for Metals, Semiconductors, Ceramics, and Polymers. *Adv. Mater.* **2008**, *20*, 1898–1904.
7. Bita, I.; Yang, J. K. W.; Jung, Y. S.; Ross, C. A.; Thomas, E. L.; Berggren, K. K. Graphoepitaxy of Self-Assembled Block Copolymers on Two-Dimensional Periodic Patterned Templates. *Science* **2008**, *321*, 939–943.
8. Ruiz, R.; Kang, H.; Detcheverry, F. A.; Dobisz, E.; Kercher, D. S.; Albrecht, T. R.; de Pablo, J. J.; Nealey, P. F. Density Multiplication and Improved Lithography by Directed Block Copolymer Assembly. *Science* **2008**, *321*, 936–939.
9. Arora, H.; Du, P.; Tan, K. W.; Hyun, J. K.; Grazul, J.; Xin, H. L.; Muller, D. A.; Thompson, M. O.; Wiesner, U. Block Copolymer Self-Assembly−Directed Single-Crystal Homo- and Heteroepitaxial Nanostructures. *Science* **2010**, *330*, 214–219.
10. Wu, N. L. Y.; Zhang, X.; Murphy, J. N.; Chai, J.; Harris, K. D.; Buriak, J. M. Density Doubling of Block Copolymer Templated Features. *Nano Lett.* **2011**, *12*, 264–268.
11. Jeong, J. W.; Park, W. I.; Kim, M.-J.; Ross, C. A.; Jung, Y. S. Highly Tunable Self-Assembled Nanostructures from a Poly-(2-vinylpyridine-*b*-dimethylsiloxane) Block Copolymer. *Nano Lett.* **2011**, *11*, 4095–4101.
12. Leibler, L. Theory of Microphase Separation in Block Copolymers. *Macromolecules* **1980**, *13*, 1602.
13. Fredrickson, G. H. Surface Ordering Phenomena in Block Copolymer Melts. *Macromolecules* **1987**, *20*, 2535–2542.
14. Ham, S.; Shin, C.; Kim, E.; Ryu, D. Y.; Jeong, U.; Russell, T. P.; Hawker, C. J. Microdomain Orientation of PS-*b*-PMMA by Controlled Interfacial Interactions. *Macromolecules* **2008**, *41*, 6431–6437.
15. Bang, J.; Jeong, U.; Ryu, D. Y.; Russell, T. P.; Hawker, C. J. Block Copolymer Nanolithography: Translation of Molecular Level Control to Nanoscale Patterns. *Adv. Mater.* **2009**, *21*, 4769–4792.
16. Albert, J. N. L.; Epps Iii, T. H. Self-Assembly of Block Copolymer Thin Films. *Mater. Today* **2010**, *13*, 24–33.

17. Thurn-Albrecht, T.; DeRouchey, J.; Russell, T. P.; Kolb, R. Pathways toward Electric Field Induced Alignment of Block Copolymers. *Macromolecules* **2002**, *35*, 8106–8110.
18. Kim, S. H.; Misner, M. J.; Xu, T.; Kimura, M.; Russell, T. P. Highly Oriented and Ordered Arrays from Block Copolymers *via* Solvent Evaporation. *Adv. Mater.* **2004**, *16*, 226–231.
19. Xuan, Y.; Peng, J.; Cui, L.; Wang, H.; Li, B.; Han, Y. Morphology Development of Ultrathin Symmetric Diblock Copolymer Film *via* Solvent Vapor Treatment. *Macromolecules* **2004**, *37*, 7301–7307.
20. Mansky, P.; Liu, Y.; Huang, E.; Russell, T. P.; Hawker, C. Controlling Polymer-Surface Interactions with Random Copolymer Brushes. *Science* **1997**, *275*, 1458–1460.
21. Ryu, D. Y.; Shin, K.; Drockenmuller, E.; Hawker, C. J.; Russell, T. P. A Generalized Approach to the Modification of Solid Surfaces. *Science* **2005**, *308*, 236–239.
22. In, I.; La, Y.; Park, S.-M.; Nealey, P. F.; Gopalan, P. Side-Chain-Grafted Random Copolymer Brushes as Neutral Surfaces for Controlling the Orientation of Block Copolymer Microdomains in Thin Films. *Langmuir* **2006**, *22*, 7855–7860.
23. Ryu, D. Y.; Wang, J.-Y.; Lavery, K. A.; Drockenmuller, E.; Satija, S. K.; Hawker, C. J.; Russell, T. P. Surface Modification with Cross-linked Random Copolymers: Minimum Effective Thickness. *Macromolecules* **2007**, *40*, 4296–4300.
24. Han, E.; In, I.; Park, S. M.; La, Y. H.; Wang, Y.; Nealey, P. F.; Gopalan, P. Photopatternable Imaging Layers for Controlling Block Copolymer Microdomain Orientation. *Adv. Mater.* **2007**, *19*, 4448–4452.
25. Han, E.; Stuen, K. O.; La, Y.; Nealey, P. F.; Gopalan, P. Effect of Composition of Substrate-Modifying Random Copolymers on the Orientation of Symmetric and Asymmetric Diblock Copolymer Domains. *Macromolecules* **2008**, *41*, 9090–9097.
26. Ji, S.; Liu, C.-C.; Son, J. G.; Gotrik, K.; Craig, G. S. W.; Gopalan, P.; Himpsel, F. J.; Char, K.; Nealey, P. F. Generalization of the Use of Random Copolymers to Control the Wetting Behavior of Block Copolymer Films. *Macromolecules* **2008**, *41*, 9098–9103.
27. Park, S.; Lee, D. H.; Xu, J.; Kim, B.; Hong, S. W.; Jeong, U.; Xu, T.; Russell, T. P. Macroscopic 10-Terabit-per-Square-Inch Arrays from Block Copolymers with Lateral Order. *Science* **2009**, *323*, 1030–1033.
28. Son, J. G.; Chang, J.-B.; Berggren, K. K.; Ross, C. A. Assembly of Sub-10-nm Block Copolymer Patterns with Mixed Morphology and Period Using Electron Irradiation and Solvent Annealing. *Nano Lett.* **2011**, *11*, 5079–5084.
29. Ikkala, O.; ten Brinke, G. Functional Materials based on Self-Assembly of Polymeric Supramolecules. *Science* **2002**, *295*, 2407–2409.
30. Yoon, J.; Lee, W.; Thomas, E. L. Highly Oriented Thin-Film Microdomain Patterns of Ultrahigh Molecular Weight Block Copolymers *via* Directional Solidification of a Solvent. *Adv. Mater.* **2006**, *18*, 2691–2694.
31. Runge, M. B.; Bowden, N. B. Synthesis of High Molecular Weight Comb Block Copolymers and Their Assembly into Ordered Morphologies in the Solid State. *J. Am. Chem. Soc.* **2007**, *129*, 10551–10560.
32. Urbas, A.; Sharp, R.; Fink, Y.; Thomas, E. L.; Xenidou, M.; Fetters, L. J. Tunable Block Copolymer/Homopolymer Photonic Crystals. *Adv. Mater.* **2000**, *12*, 812–814.
33. Kang, Y.; Walish, J. J.; Gorishnyy, T.; Thomas, E. L. Broad-Wavelength-Range Chemically Tunable Block-Copolymer Photonic Gels. *Nat. Mater.* **2007**, *6*, 957–960.
34. Kim, G.; Libera, M. Morphological Development in Solvent-Cast Polystyrene-Polybutadiene-Polystyrene (SBS) Triblock Copolymer Thin Films. *Macromolecules* **1998**, *31*, 2569–2577.
35. Ludwigs, S.; Boker, A.; Voronov, A.; Rehse, N.; Magerle, R.; Krausch, G. Self-Assembly of Functional Nanostructures from ABC Triblock Copolymers. *Nat. Mater.* **2003**, *2*, 744–747.
36. Jung, Y. S.; Ross, C. A. Solvent-Vapor-Induced Tunability of Self-Assembled Block Copolymer Patterns. *Adv. Mater.* **2009**, *21*, 2540–2545.
37. Chen, Y.; Huang, H.; Hu, Z.; He, T. Lateral Nanopatterns in Thin Diblock Copolymer Films Induced by Selective Solvents. *Langmuir* **2004**, *20*, 3805–3808.
38. Peng, J.; Wei, Y.; Wang, H.; Li, B.; Han, Y. Solvent Induced Sphere Development in Symmetric Diblock Copolymer Thin Films. *Macromol. Rapid Commun.* **2005**, *26*, 738–743.
39. Harrison, C.; Adamson, D. H.; Cheng, Z.; Sebastian, J. M.; Sethuraman, S.; Huse, D. A.; Register, R. A.; Chaikin, P. M. Mechanisms of Ordering in Striped Patterns. *Science* **2000**, *290*, 1558–1560.
40. Kim, B. H.; Lee, H. M.; Lee, J.-H.; Son, S.-W.; Jeong, S.-J.; Lee, S.; Lee, D. I.; Kwak, S. U.; Jeong, H.; Shin, H. *et al.* Spontaneous Lamellar Alignment in Thickness-Modulated Block Copolymer Films. *Adv. Funct. Mater.* **2009**, *19*, 2584–2591.
41. Zhang, X.; Harris, K. D.; Wu, N. L. Y.; Murphy, J. N.; Buriak, J. M. Fast Assembly of Ordered Block Copolymer Nanostructures through Microwave Annealing. *ACS Nano* **2010**, *4*, 7021–7029.
42. Pargellis, A. N.; Finn, P.; Goodby, J. W.; Panizza, P.; Yurke, B.; Cladis, P. E. Defect Dynamics and Coarsening Dynamics in Smectic-C Films. *Phys. Rev. A* **1992**, *46*, 7765–7776.
43. Barrat, J. L.; Fredrickson, G. H. Diffusion of a Symmetric Block Copolymer in a Periodic Potential. *Macromolecules* **1991**, *24*, 6378–6383.
44. Whitmore, M. D.; Noolandi, J. Self-Consistent Theory of Block Copolymer Blends: Neutral Solvent. *J. Chem. Phys.* **1990**, *93*, 2946–2955.
45. Kim, S. O.; Solak, H. H.; Stoykovich, M. P.; Ferrier, N. J.; de Pablo, J. J.; Nealey, P. F. Epitaxial Self-Assembly of Block Copolymers on Lithographically Defined Nanopatterned Substrates. *Nature* **2003**, *424*, 411–414.
46. Stoykovich, M. P.; Müller, M.; Kim, S. O.; Solak, H. H.; Edwards, E. W.; de Pablo, J. J.; Nealey, P. F. Directed Assembly of Block Copolymer Blends into Nonregular Device-Oriented Structures. *Science* **2005**, *308*, 1442–1446.
47. Cheng, J. Y.; Ross, C. A.; Smith, H. I.; Thomas, E. L. Templated Self-Assembly of Block Copolymers: Top-Down Helps Bottom-Up. *Adv. Mater.* **2006**, *18*, 2505–2521.
48. Park, S. M.; Stoykovich, M. P.; Ruiz, R.; Zhang, Y.; Black, C. T.; Nealey, P. F. Directed Assembly of Lamellae- Forming Block Copolymers by Using Chemically and Topographically Patterned Substrates. *Adv. Mater.* **2007**, *19*, 607–611.
49. Han, E.; Kang, H.; Liu, C.-C.; Nealey, P. F.; Gopalan, P. Graphoepitaxial Assembly of Symmetric Block Copolymers on Weakly Preferential Substrates. *Adv. Mater.* **2010**, *22*, 4325–4329.
50. Galatsis, K.; Wang, K. L.; Ozkan, M.; Ozkan, C. S.; Huang, Y.; Chang, J. P.; Monbouquette, H. G.; Chen, Y.; Nealey, P.; Botros, Y. Patterning and Templating for Nanoelectronics. *Adv. Mater.* **2010**, *22*, 769–778.
51. Jeong, S.; Moon, H.-S.; Kim, B. H.; Kim, J. Y.; Yu, J.; Lee, S.; Lee, M. G.; Choi, H.; Kim, S. O. Ultralarge-Area Block Copolymer Lithography Enabled by Disposable Photoresist Prepatterning. *ACS Nano* **2010**, *4*, 5181–5186.
52. Jeong, S.; Moon, H.; Shin, J.; Kim, B. H.; Shin, D. O.; Kim, J. Y.; Lee, Y.-H.; Kim, J. U.; Kim, S. O. One-Dimensional Metal Nanowire Assembly *via* Block Copolymer Soft Graphoepitaxy. *Nano Lett.* **2010**, *10*, 3500–3505.
53. Seh-Won, A.; Ki-Dong, L.; Jin-Sung, K.; Sang Hoon, K.; Joo-Do, P.; Sarng-Hoon, L.; Phil-Won, Y. Fabrication of a 50 nm Half-Pitch Wire Grid Polarizer Using Nanoimprint Lithography. *Nanotechnology* **2005**, *16*, 1874.
54. Liu, X.; Deng, X.; Sciortino, P.; Buonanno, M.; Walters, F.; Varghese, R.; Bacon, J.; Chen, L.; O'Brie, N.; Wang, J. J. Large Area, 38 nm Half-Pitch Grating Fabrication by Using Atomic Spacer Lithography from Aluminum Wire Grids. *Nano Lett.* **2006**, *6*, 2723–2727.